energies

MDPI

Article

Comprehensive Thermodynamic Evaluation of the Natural Gas-Fired Allam Cycle at Full Load

Lorenzo Colleoni, Alessio Sindoni and Silvia Ravelli *

Department of Engineering and Applied Sciences, University of Bergamo, Viale Marconi 5, 24044 Dalmine, Italy; l.colleoni7@studenti.unibg.it (L.C.); a.sindoni2@studenti.unibg.it (A.S.)
* Correspondence: silvia.ravelli@unibg.it; Tel.: +39-035-2052346

Abstract: In this study, thermodynamic modeling and simulations were used to optimize the design point performance of the Allam cycle. The topic fits perfectly with the strategies for power sector decarbonization toward net zero emission. In fact, it offers an environmentally friendlier alternative to natural gas combined cycle (NGCC) plants. The focus is on oxyfuel combustion that, combined with supercritical CO_2 (sCO_2) stream as working fluid, produces high-purity CO_2, electricity, and water by means of a highly recuperated Brayton cycle. The former is ready for sequestration, pipeline injection, or other applications, such as enhanced oil recovery or industrial processes. Being designed within the last decade, large-scale plants are poorly documented in the published literature and not yet ready for operation. Accordingly, a thermodynamic model was developed for a net power (P_n) output of 300 MW. After validation against the little data available from academic studies, simulation sets were conceived to assess the impact of main process parameters on cycle efficiency. To that end, operating conditions of the compressor, turbine, and air separation unit (ASU) were varied in a parametric analysis, preparatory to performance optimization. For the chosen layout, the maximum net electric efficiency ($\eta_{el,n}$) was found to be 50.4%, without thermal recovery from ASU.

Keywords: Allam cycle; decarbonization; thermodynamic modeling; net electric efficiency

Citation: Colleoni, L.; Sindoni, A.; Ravelli, S. Comprehensive Thermodynamic Evaluation of the Natural Gas-Fired Allam Cycle at Full Load. *Energies* **2023**, *16*, 2597. https://doi.org/10.3390/en16062597

Academic Editor: Ron Zevenhoven

Received: 1 February 2023
Revised: 2 March 2023
Accepted: 7 March 2023
Published: 9 March 2023

1. Introduction

According to a recent report from the International Energy Agency, the largest growth in CO_2 emissions by sector in 2021 took place in electricity and heat production, thus accounting for 46% of the global rise in emissions [1]. That is because the rapid surge in global electricity demand after the pandemic was met mainly by fossil fuels: in particular, more coal was burned despite the largest ever annual increase in renewable power generation, thanks to solar and wind technology. Additionally, natural gas (NG) demand increased in all sectors [2]. Coal and gas covered about 60% of the global electricity generation in 2021, whereas total clean sources stood at the remaining fraction of 40%, including nuclear source [3]. There has been insufficient progress in decarbonizing the energy sector: the transition process is still too slow to put global emissions into sustained decline towards net zero. As long as the increase in renewable generation capacity is less than the augmentation in global energy demand, fossil fuels will not be phased out anytime soon. Holechek et al. [4] sought to identify the conditions for a complete replacement of fossil fuels with renewable energy by 2050. They set up a long list in which key points are the following: worldwide energy demand should not exceed by more than 25% the current level, renewable energy should be exploited at six to eight times the present rate, nuclear power should be increased by at least 30%, and carbon capture and storage (CCS) should be widely applied. However, the penultimate point brings several issues dealing with high costs and long time for plant construction, large needs of water for cooling purposes, hazardous waste disposal, and safety and public confidence [5]. As regards CCS, the main challenges relate to high capital investment and lack of both financial incentives

for CO_2 geological storage and consistent regulations, besides low public acceptance [6]. Even in the most optimistic scenario by 2050, traditional fuels are essential as a backup when renewables inevitably fail, in order to ensure reliable energy services. NG, being the cleanest, has strong medium-to-long-term future as balancing fuel; nonetheless, the issue of intermittency is expected to dissipate in time as the system evolves through the development of large-scale battery storage and distributed generation deployment. If methane is decarbonized, then its contribution to electricity generation will remain significant in the coming decades [7]. On the one hand, post-combustion technology is considered the most viable method for CO_2 reduction in existing power plants [8]. On the other hand, the development of unconventional thermodynamic cycles for clean power generation from NG would constitute an alternative approach. Research areas of potential interest include land-based gas turbine cycles with inherent carbon capture ability, by means of oxyfuel combustion [9].

Among the oxyfuel power cycles, the Allam cycle [10] is one of the most promising due to its high efficiency combined with zero greenhouse gas emissions [11] and capability to produce pipeline-ready CO_2 [12]. In short, it is a semi-closed, intercooled, and highly regenerative oxy-combustion Brayton cycle that uses sCO_2 as working fluid. The base project was developed by 8 Rivers Capital and commercialized by NET Power, LLC, in partnership with Toshiba Corporation, Exelon Corporation, and CB&I [13]. The original design of the cycle fed by NG included a fuel compressor, combustor, ASU, turbine, multistream recuperator, oxidant pump, water separator, two-stage CO_2 compressor with intercooling, and recycled CO_2 flow pump. The first-of-a-kind plant in La Porte, Texas, is a 50 MW_{th} (25-MW_{el}) unit where testing campaigns with NG have been ongoing since May 2018. The design for a 300 MW NG-fired power plant is under development: construction near Odessa (Texas) is slated to begin in the third quarter of 2024, and NET Power is targeting commissioning in the third quarter of 2026, according to the latest reports [14]. In one of the earliest studies, which dates back to 2013, Allam et al. [15] declared a net efficiency of $\eta_{el,n}$ = 58.9% based on the lower heating value (LHV) of the fuel, i.e., NG. This value is actually comparable to that of the current NGCC technology. They also stated that the cost of electricity with 100% capture of emissions can be highly competitive with the best solutions available that do not employ carbon capture. Mancuso et al. [16] conducted an independent cost analysis that brought a specific cost of 1068 €/kW for a system with full CO_2 capture at pipeline conditions, which is in close agreement with NET Power's estimated value of 992 €/kW. They pointed out that the Allam cycle requires fewer and smaller turbines compared with NGCC, without the complexity of the heat recovery steam generator: a single turbine per train can be used, instead of two gas turbines and three steam turbines. A year later, Allam et al. [17] provided a detailed explanation of the cycle thermodynamic characteristics, pointing out how and why it is distinct from other carbon dioxide cycles.

The following efforts were devoted to designing the most critical components, such as compressor [18], combustor [19,20], cooled turbine [20], and heat exchangers [21]. At the same time, methods of modelling were proposed to properly simulate the Allam cycle in various aspects. White and Weiland [22] compared 10 different physical property methods for modeling direct fired sCO_2 cycles in Aspen Plus®: REFPROP was found to grant the highest level of accuracy over a wide range of streams, including saturated liquid and vapor states of pure CO_2, superheated CO_2 vapor, and vapor/liquid equilibria of CO_2–H_2O mixtures. Thermodynamic investigations were carried out by Haseli [23–25] with the twofold aim of better understanding the physics of the Allam cycle and optimizing its efficiency under simplifying assumptions. Note that neither intercooling for fuel and CO_2 compressors nor turbine cooling was accounted for. Furthermore, all components were operated adiabatically. An analytical expression for P_n was derived in [23], where turbine inlet temperature (TIT), turbine inlet pressure (TIP), and turbine outlet pressure (TOP) were selected as the most relevant parameters affecting cycle performance. The calculation algorithm presented in [24] unveiled that cycle efficiency shows a global maximum if

it is optimized with respect to both TIP and TOP at a given combustor temperature. Algebraic relations for determining the optimal values of TIT, TIP, and TOP, which attain the maximum $\eta_{el,n}$, were reviewed in [25]. An optimized cycle design was outlined, with TIT = 1306 K, TIP = 300 bar, and TOP = 39.4, thus reaching an impressive $\eta_{el,n}$ of 66.4%, albeit with some ideal features. Similarly, both sensitivity analysis and design optimization were implemented by Scaccabarozzi et al. [26]: the resulting maximum $\eta_{el,n}$ of 54.8% reaffirms the outstanding performance of the Allam cycle with 100% CO_2 capture but prompts questions as regards the ability to estimate the realistic limits of $\eta_{el,n}$. Indeed, hypotheses held in [26] are closer to reality compared with [23–25], especially because of a cooled turbine model. The same is valid for [27], in which a stage-by-stage approach was adopted to compute the amount of cooling flow needed by the turbine. Moreover, attention was paid in detail, thus considering isentropic efficiency (η_{is}) of turbines and compressors, additional losses for generator and transformer, and pressure losses. All this translated into a lower $\eta_{el,n}$ value (52.4%) than in [26].

Modifications to the first version of the cycle were introduced and simulated for various purposes. Mitchell et al. [28] focused on a flexible operation of Allam power plants when included in the Great Britain electricity system. A liquid oxygen storage was added to the cycle with the aim of decoupling power generation from oxygen production, thus removing the dynamic constraints of ASU (which has, in fact, the lowest ramp rate). The impact of ASU on $\eta_{el,n}$ was addressed in [29]: a genetic algorithm optimization was used to maximize $\eta_{el,n}$ with and without the heat transfer from the ASU compressors to the recuperator. It was found that $\eta_{el,n}$ increases by 6 percentage points (pp) with full heat integration, thus showing the potential of an on-site ASU.

With the goal of pursuing the highest efficiency and the lowest emission level, the Allam cycle was compared against other power cycles with CO_2 recirculation, such as a semi-closed oxyfuel combustion combined cycle and the E-MATIANT cycle [30]. After a parametric optimization of each cycle, the Allam cycle proved to be the most effective oxyfuel technology in terms of $\eta_{el,n}$. This was also confirmed when the comparison was extended to other solutions, such as the Graz cycle and CES cycle [31]. The best efficiency is combined with a CO_2 emission of only 4 g/kWh.

From literature review, it appears clear that the reported $\eta_{el,n}$ for the NG-fired Allam cycle covers a wide range of values. In most studies, the optimized $\eta_{el,n}$ is lower than that declared by developers. It is also true that modelling assumptions have a deep impact on $\eta_{el,n}$, so the discrepancies in cycle layout, target power output, and equation of state calculations may provide sufficient reasoning. The main goal of this work is to predict the steady-state operation of the NG-fired Allam cycle in view of upcoming applications. Hence, the original project [21] has been tailored to the next "serial number one" installation, citing NET power [14], thus considering flexible options for heat recovery and oxygen supply, commercially available components, and realistic energy losses with a target of 300 MW power output. This practical approach may provide a more realistic assessment of the Allam cycle potential than the abovementioned studies, although the methodology applied is drawn from the literature. A fair comparison with NGCC would be established based on operational reality.

With the help of a simulation tool, a base case was conceived in accordance with the guidelines contained in [21] by integrating supplemental information from [26,28]. The model outcomes were verified against the results obtained in previous studies by varying the most significant thermodynamic parameters within an acceptable range. This was the base for the optimized case, in which the maximum $\eta_{el,n}$ is searched as dependent on a list of decision variables including TIP, TIT, and TOP.

2. Thermodynamic Model and Assumptions

This section aims to retrace the steps taken to simulate the nominal operation of the Allam cycle, starting from information made public by the developers. The model was built in Thermoflex® (Version 30, Thermoflow Inc., Jacksonville, FL, USA) by con-

necting components in a graphic interface. Heat and mass balances were solved on the basis of input parameters for each component; outputs, such as pressure, temperature, enthalpy, and mass flow rate, were iteratively computed until their values converged on a final solution with a tolerance of 5×10^{-5}. The number of computed loops varied between 30 and 500. An additional convergence check, with a tolerance of 0.01%, was made on plant gross power. The NIST Reference Fluid Thermodynamic and Transport Properties Database (REFPROP) provided accurate thermophysical properties for CO_2 streams.

The process flow diagram reported in [21] and here shown in Figure 1 for convenience was taken as a reference. A single turbine generates power, with a TIP of about 300 bar and a pressure ratio of 10. Pressurized NG (14) is burned under lean conditions in the presence of a high-temperature oxidizing mixture consisting of the following: CO_2; pure oxygen (13), produced by a co-located ASU; an additional flow of recirculated CO_2 (9) at high temperature and pressure, acting as a diluent to reduce combustion temperature and hence TIT down to 1150 °C. The exhaust flow exiting the combustor is expanded through the turbine, thus lowering its pressure and temperature to about 30 bar and 700 °C, respectively (1). Turbine outlet flow is conveyed to the recuperator, where it transfers heat to oxidant flow and recycle stream. It is then cooled near ambient temperature, and water deriving from the combustion process is separated (3). The resulting stream, which is mainly composed of CO_2, is then recompressed (4), cooled (7), and pumped to 300 bar so as to re-enter the cold end of the recuperator. Upstream of the recuperator, part of the recirculating CO_2 is combined with O_2 (11) to form an oxidizing mixture (12), which is sent separately to both the heat exchanger and the turbine. Inside the recuperator, the recycle flows are preheated in countercurrent by the exhaust of the turbine, thus returning to the combustor at temperatures above 700 °C. In order to ensure mass balance, a part of the pure CO_2 is exported for sequestration or downstream usage. It accounts for roughly 5% of overall recycle stream, thus meaning that the process is almost closed. For the sake of clarity, the operating conditions indicated in [21] are collected in Table A1 in terms of pressure and temperature. The key aspects of the modeled power cycle are hereafter described with reference to Figure 2, in which the final layout is depicted.

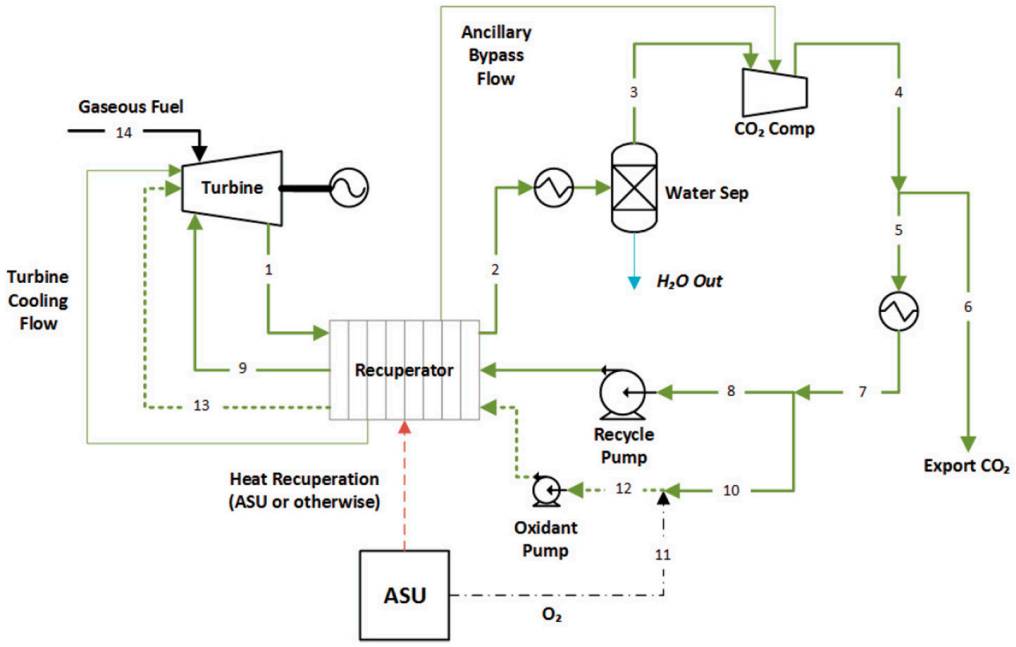

Figure 1. Layout of a simplified commercial-scale natural gas Allam cycle [21], with stream numbers.

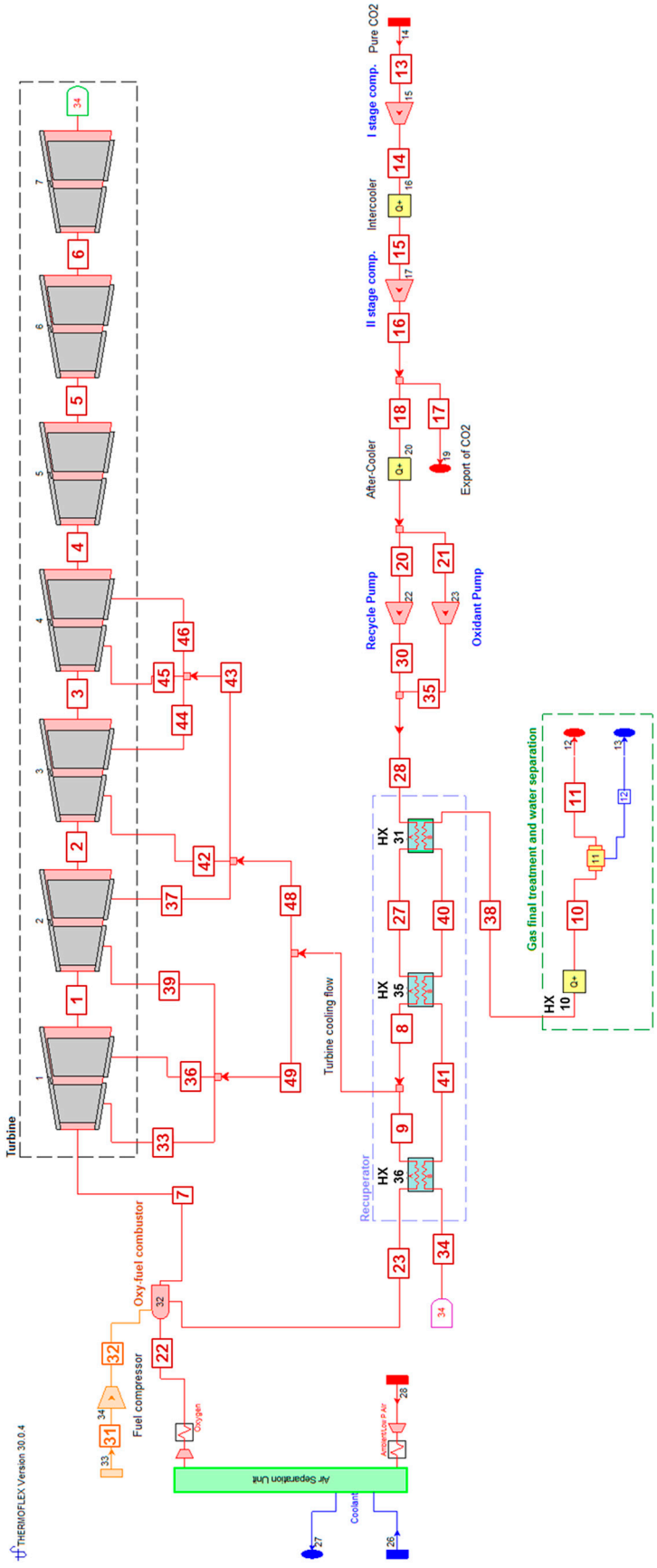

Figure 2. Schematic diagram of the natural gas-fired Allam cycle (component numbers are written in black; stream numbers are indicated in red/orange boxes).

2.1. Turbine

Scaccabarozzi et al. [26] used a modified version of El-Masri's continuous expansion model [32]. Similarly, the cooled (gas) turbine icon available in Thermoflex relies on El-Masri's code, known as GASCAN [33]. Entropy production in gas expansion contains contributions from:

- Friction and aerodynamic losses in the main gas path, quantified by turbine polytropic efficiency ($\eta_{y,t}$);
- Throttling of cooling air from its supply pressure to the local pressure;
- Irreversible heat transfer from gas to coolant, followed by mixing of coolant and gas: this mixing process causes further heat transfer irreversibility in bringing the mixture to a common temperature, as well as an irreversible loss of stagnation pressure to accelerate the coolant to the main flow velocity.

Therefore, despite the lack of accessible knowledge about the cooling flow rate, the coolant flow interaction with the mainstream must be considered for accuracy. In this specific case, CO_2 is an excellent coolant fluid, having very high heat transfer capability because of its high pressure and its own physical properties. In particular, the cooled turbine stage behavior assumed here is illustrated in Figure 3. The total enthalpy drop is due to cooling (see A−B and C−D) and work extraction (B−C), as qualitatively presented in Figure 3a and clearly indicated in Figure 3b. The latter was computed as shown by the solid line B−C: the effective total pressure ratio is reduced because of upstream and downstream coolant mixing with the main flow, but the stage total-to-total efficiency (η_{TT}) is unaltered, i.e., the same as that without film cooling; thus:

$$T_B - T_C = \eta_{TT}\, T_B \left[1 - \frac{p_C}{p_B}\right]^{\frac{\gamma-1}{\gamma}} \quad (1)$$

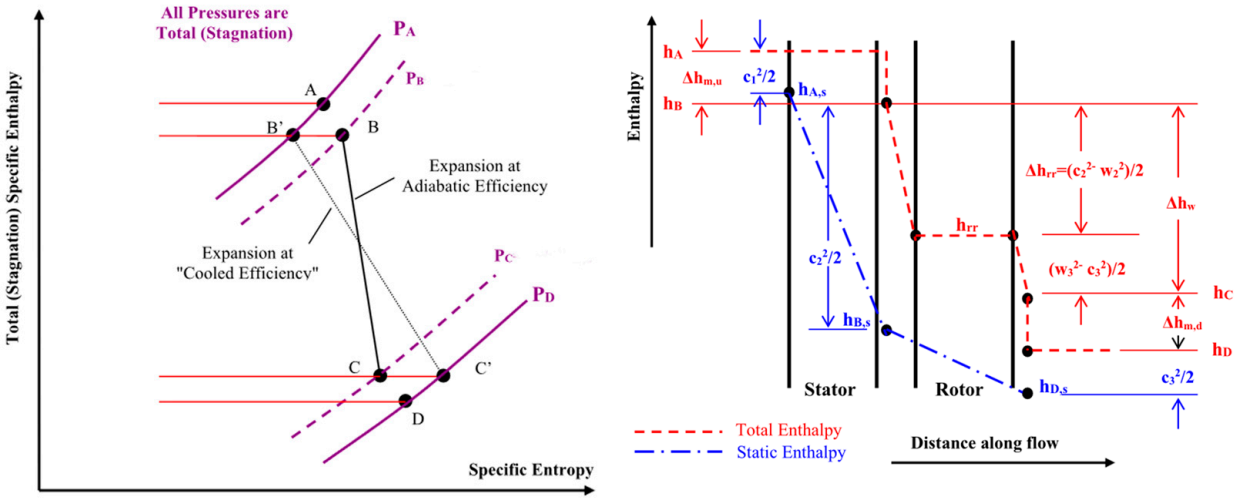

Figure 3. Cooled turbine stage model [34]: (**a**) graphical representation of the expansion line; (**b**) total and static states.

Seven cooled turbine stages were used to model the turbine designed by Toshiba [20], the first four being cooled (see turbine block in Figure 2). This is valid for both rotational and stationary parts. Each stage consists of four cooled elements: stator row, rotor row, forward wheelspace, and aft wheelspace. The endwall cooling flows are included with their associated blade rows. Transition piece leakage flows are included with the first-stage

nozzle flow. The cooling flows to each blade row are calculated from a semiempirical cooling effectiveness relation available in [33]:

$$\frac{(mc_p)_{cf}}{(mc_p)_g} = \alpha\left(\frac{\phi}{\phi_\infty - \phi}\right)^z \quad (2)$$

where the expression on the left is the coolant-to-mainstream heat capacity ratio, and ϕ denotes the cooling effectiveness:

$$\phi = \frac{T_g - T_w}{T_g - T_{cf}} \quad (3)$$

T_g is the adiabatic wall temperature of the hot gas, taken as the incoming gas stagnation temperature for the stator and the incoming gas rotor-relative stagnation temperature for the rotor. T_w and T_{cf} are the blade surface temperature and the coolant temperature, respectively. The maximum cooling effectiveness ϕ_∞ refers to infinitely large coolant flow rates, whereas α and z are correlation coefficient and exponent, respectively. Values of ϕ_∞, α, and z can be adapted to match experimental curves, if available.

Thermal barrier coating (TBC) was also included for both stator and rotor blade rows. The right-hand side of Equation (2) is modified by the addition of a correction factor μ as follows:

$$\frac{(mc_p)_{cf}}{(mc_p)_g} = \mu\alpha\left(\frac{\phi}{\phi_\infty - \phi}\right)^z \quad (4)$$

It mainly depends on the square root of the coating thickness parameter (Th):

$$Th = \left(\frac{th}{cs}\right)\left(\frac{\lambda_g}{\lambda_{TBC}}\right) \quad (5)$$

where th/cs is the dimensionless coating thickness, defined as the ratio of the coating thickness (th) to the length of cooled surface interval (cs), and λ_g/λ_{TBC} is the ratio between the thermal conductivity of gas flow (λ_g) and that of coating (λ_{TBC}). Cooling parameters were chosen on the basis of F class gas turbines (Table 1). The design metal temperature was set at 860 and 843 °C for stator and rotor, respectively.

Table 1. Cooling parameters chosen for the turbine model.

	α	z	ϕ_∞	th/cs	λ_{TBC} (kW/(m °C))
Stator-convective cooling	0.064	1.25	0.85	0.008	0.002
Rotor-convective cooling	0.0576	1.25	0.85	0.008	0.002
Stator-film cooling	0.05	0.9	1	0.008	0.002
Rotor-film cooling	0.04	0.9	1	0.008	0.002

Stage uncooled adiabatic efficiency was assumed to progressively increase from the first to the seventh stage in the range between 90% and 93%. This differs from the hypothesis of equal η_{is} for all stages made by Mitchell et al. [28].

2.2. Recuperator

The transfer of heat between the turbine exhaust (hot side) and the recirculated stream (cold side) is deeply affected by the nonlinear variation of the CO_2 working fluid's heat capacity with pressure and temperature, with the latter ranging from 700 to 40 °C (Figure 4). On the hot side, flue gas, at a pressure of approximately 30 bar, contains 93% vol of CO_2 and 7% vol of H_2O: specific heat capacity (c_p) slightly declines with temperature from 1.2 to 1 kJ/(kg °C). On the cold side, pure CO_2 at 300 bar heats up with a greater change in c_p, which drops from about 2 to 1.3 kJ/(kg °C). Specific solutions were suggested to model the recuperator, taking into consideration streams with variable c_p: two multiflow heat exchangers in series were designed in [26], whereas Mitchell et al. [28] divided the heat

exchange system into a pair of two-stream and a pair of multiflow heat exchangers. Each of the four heat exchangers was then discretized in a finite number of ideal heat exchange steps. Furthermore, the condensation of water below the dew point of the exhaust flow should be kept in mind.

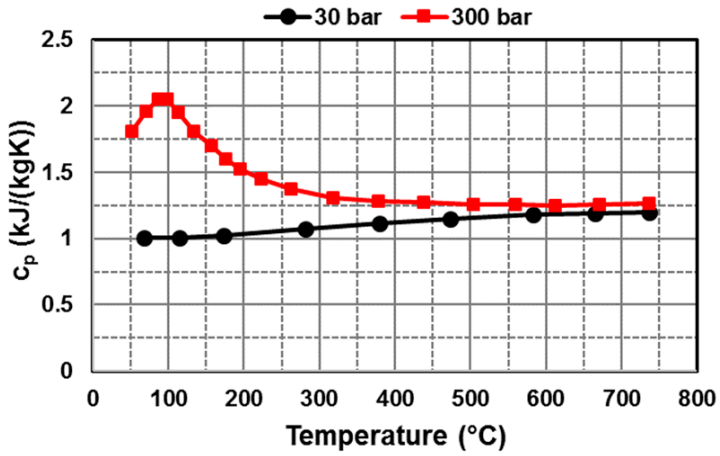

Figure 4. Variation of CO_2 heat capacity with pressure and temperature across the recuperator.

In this study, the approach proposed in [28] was adapted to comply with Thermoflex configuration. Specifically, three (two-stream) heat exchangers were arranged in series, as shown in Figure 2, to achieve the correct values of temperature difference on each side, consistent with [21,26,28]. The recirculated CO_2 enters the recuperator at heat exchanger #31, where the outlet temperature of exhaust gas is set at 40 °C with a minimum pinch of 2 °C. For the remaining heat exchangers (#35 and #36), thermal effectiveness is set at 98%. Pressure drop across each heat exchanger, on both sides, was assumed equal to dp/p = 2% according to the following:

$$\frac{dp}{p} = \frac{p_{in}}{p_{out}} - 1 \quad (6)$$

where p_{in} and p_{out} are the pressure values before and after the loss, respectively.

Thermal recovery from ASU's main air compressor and booster compressor was not considered, since a devoted co-located ASU might not be available. Indeed, oxygen can be supplied by a pipeline from an adjacent air separation plant, as in the case of the demonstration plant [21]. In addition, the first commercial 300 MW power plant by NET Power will include a "commercially available" ASU, with multistage compression and water intercooling [35].

Downstream of the heat recovery process, flue gas undergoes a further cooling step, thus reducing its temperature from about 40 to 17 °C through the heat removal icon (10) with an additional pressure drop of dp/p = 2%. The cold source is not mentioned in [21], but chilled water can be a reasonable assumption. A moisture separator (11) removes liquid water from gas flow: condensed water and pure CO_2 are sent to separate sinks: (13) and (12), respectively. It is worth noting that pressure drops across heat exchangers #36, 35, 31, and 10 make the flue gas pressure decrease from 31.4 bar at the turbine outlet to 29 bar at the inlet of the compression section.

2.3. CO_2 Compression

Recirculated CO_2 compression was divided in the following steps according to the guidelines provided in [21]:

- Intercooled two-stage compression up to 80 bar, i.e., above the critical point;
- Export of excess CO_2 amounting to 3% of the total recycle flow (please note that sink (12) and source (14) ensure compliance with the mass balance);

- Cooling of the sCO_2 stream to near ambient temperature, so density is raised by a factor of 5, thus reaching approximately 850 kg/m^3 at the inlet of the dense phase pump;
- Final compression to about 300 bar by means of two pumps connected in parallel to mimic the "recycle pump" and the "oxidant pump" of Figure 1.

Nevertheless, in Figure 2, oxygen is fed directly to the combustor.
A pressure drop of dp/p = 2% was set across intercooler and aftercooler.

2.4. ASU and Combustor

The task of ASU is to supply the combustor with a stable flow of high-pressure, high-purity (99.5%) oxygen. Although a conventional double distillation column system can be used, operating data are not available. Thus, the cryogenic distillation process was modelled as a black box: conditions related to air/oxygen compression and distillation column were tuned to attain an ASU consumption in line with the literature. This is consistent with the approach taken in [26–28]. Specifically, a multistage intercooled compression configuration was chosen for both ambient air and oxygen with a compressor polytropic efficiency of $\eta_{y,c}$ = 90%. In the former case, two stages are required to increase air pressure from ambient level to that of the distillation column, set at 4.4 bar. In the latter case, five stages are needed to raise oxygen pressure from 4.4 to slightly above 300 bar. The pressure ratio of each stage is between 2.2 and 2.5 so that the discharge temperature for all stages does not exceed 120 °C. Water cooling applies to all inter-/aftercoolers: cooling water is available at 15 °C, and its temperature increases by 10 °C. The resulting specific power consumption of 1326 kJ/kg$_{O2}$ is reasonable in the light of the values reported in [26,28], equal to 1391 and 1354 kJ/kg$_{O2}$, respectively.

Pure oxygen from ASU enters the combustor together with fuel and recirculating CO_2. At the outlet, a gas stream with almost zero oxygen content was obtained at the assigned exit temperature. The amount of oxygen required from the ASU depends on the minimum oxygen concentration in flue gas, set to zero.

3. Model Validation and Sensitivity Analysis

Validation of the base-case model presented in Section 2 was carried out with the twofold purpose of assessing the simulation outputs against the expected cycle performance and evaluating the impact of main cycle parameters on $\eta_{el,n}$.

3.1. Base-Case Model Validation

Table 2 contains the information available for verifying the accuracy of the proposed Thermoflex model (indicated hereafter as TFX). Values of pressure, temperature, and mass flow rate were found to match those taken from [6] very closely. The largest deviation between predicted and reference parameters is less than 4%. This discrepancy is acceptable to consider the cycle simulation reliable, even considering that turbomachinery efficiency was estimated on the basis of both engineering practices and theoretical studies [26,28]. This is especially true for turbine outlet temperature (TOT), which depends on the assessment of several unknown parameters related to the cooled expansion, as explained in Section 2.1. For a full characterization of the base-case cycle operation, the reader is referred to the left column of Table A2.

Table 2. Validation of the base-case model.

Parameter	TFX	Data from [6]	Δ%
Turbine inlet pressure (bar)	292	300	2.67
Turbine inlet temperature (°C)	1158	1158	-
Turbine outlet pressure (bar)	31	30	3.30
Turbine outlet temperature (°C)	706	727	2.89
Minimum cycle temperature (°C)	17	17	-
Turbine coolant mass fraction (%)	11	11.3	0.30
Turbine exhaust flow (kg/s)	939	923	1.73
ASU penalty (%LHV)	10.64	10.95	0.31

As regards the power production, the computed P_n of 281 MW was lower than the reference value of 300 MW. However, developers did not disclose generator and transformer losses that were nevertheless included in the model. The predicted $\eta_{el,n}$ of 49% was also underestimated compared with the expected level of 58.9% [15]. Indeed, to the authors' knowledge, none of the studies in the published literature delivered $\eta_{el,n}$ as high as that declared by NET Power. Moreover, $\eta_{el,n}$ of 48.4% was computed in [29] for a system without thermal recovery from ASU under the conditions reported in [21], thus reinforcing the validity of this study.

3.2. Sensitivity Analysis

The key cycle parameters were varied while searching for the maximum $\eta_{el,n}$. One parameter was varied at a time, everything else being equal. Specifically, attention was drawn to TIT, TIP, TOP, and η_{is} of turbomachinery and ASU-specific consumption. Results from this study were compared with those computed by Scaccabarozzi et al. [26], despite the difference in size, main design parameters, and heat recovery mode across the recuperator. In fact, they modelled a larger power plant with heat recovery from ASU to produce a P_n of 419 MW in the base case. Consequently, it was necessary to adopt a dimensionless representation of data for a proper validation. As shown in Figures 5–9, each decision variable reported on the *x*-axis was divided by its optimal value, i.e., that attaining the highest $\eta_{el,n}$. The corresponding values of the objective function ($\eta_{el,n}$), shown on the *y*-axis, were divided by the maximum $\eta_{el,n}$. The same was performed when plotting the net specific work (W_n). A good match between the reported curves suggests that the thermodynamic behavior has been accurately simulated in this work, although the absolute value of the parameters involved is different from that in [26].

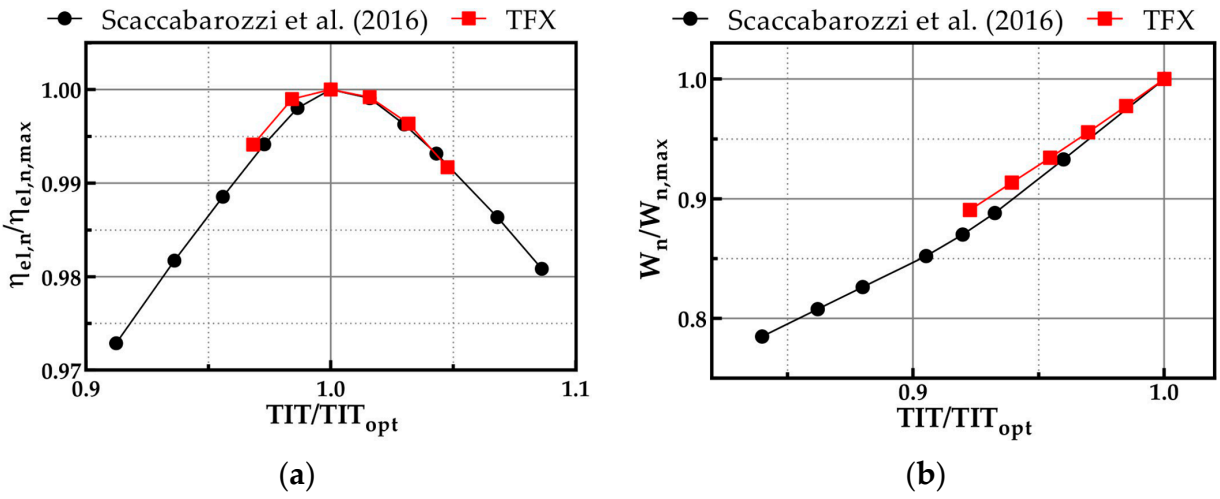

Figure 5. Allam cycle performance as a function of turbine inlet temperature: (**a**) net electric efficiency; (**b**) net specific work. Validation against Scaccabarozzi et al., thermodynamic analysis, and numerical optimization of the NET Power oxy-combustion cycle [26].

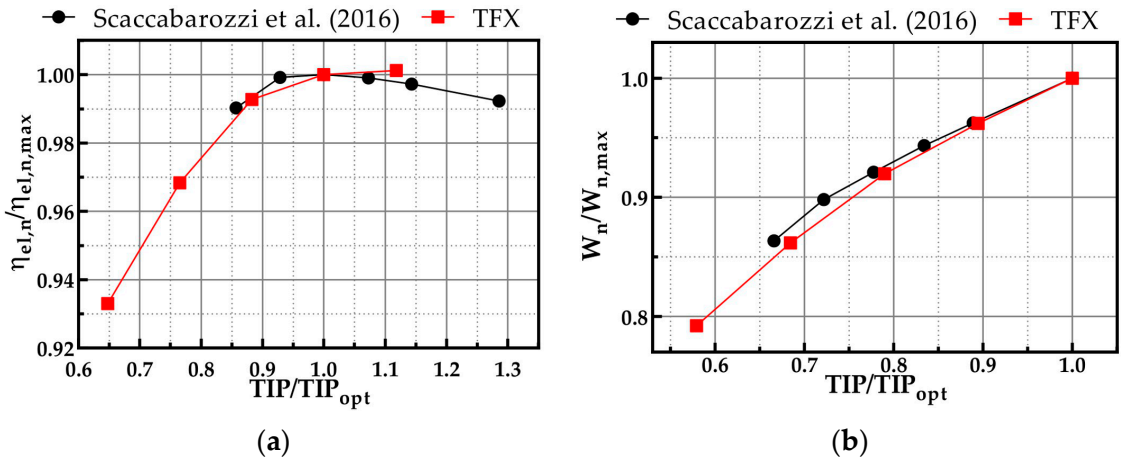

Figure 6. Allam cycle performance as a function of turbine inlet pressure: (**a**) net electric efficiency; (**b**) net specific work. Validation against Scaccabarozzi et al., thermodynamic analysis, and numerical optimization of the NET Power oxy-combustion cycle [26].

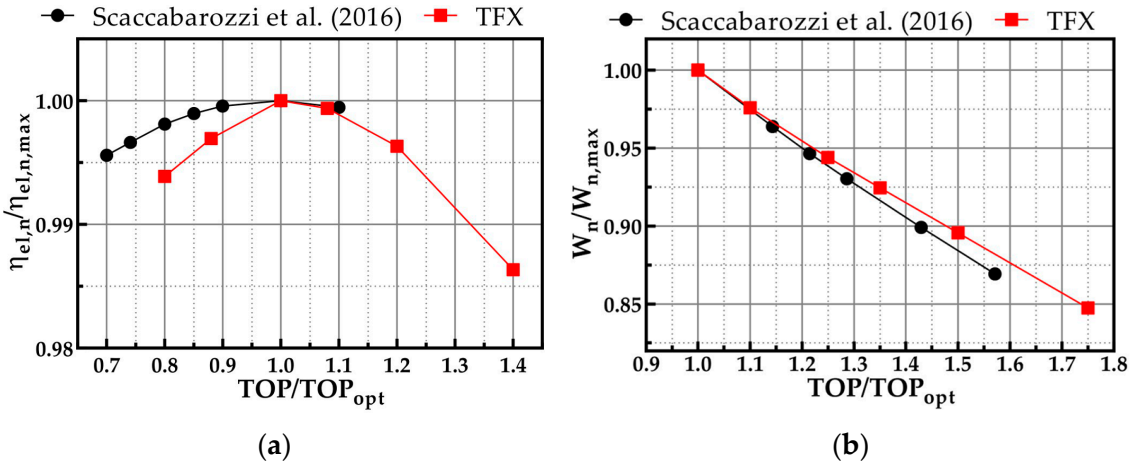

Figure 7. Allam cycle performance as a function of turbine outlet pressure: (**a**) net electric efficiency; (**b**) net specific work. Validation against Scaccabarozzi et al., thermodynamic analysis, and numerical optimization of the NET Power oxy-combustion cycle [26].

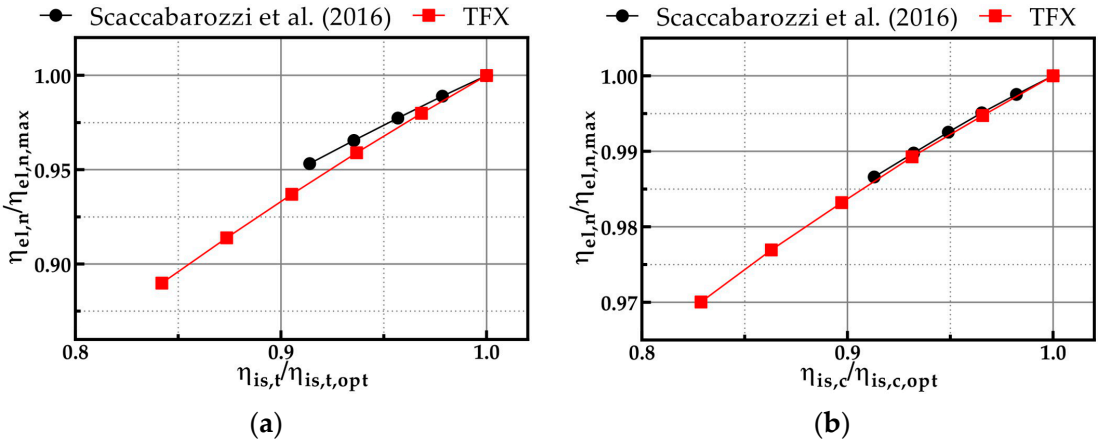

Figure 8. Net electric efficiency of the Allam cycle as a function of turbomachinery efficiency: (**a**) isentropic efficiency of turbine stages; (**b**) isentropic efficiency of CO_2 compressors. Validation against Scaccabarozzi et al., thermodynamic analysis, and numerical optimization of the NET Power oxy-combustion cycle [26].

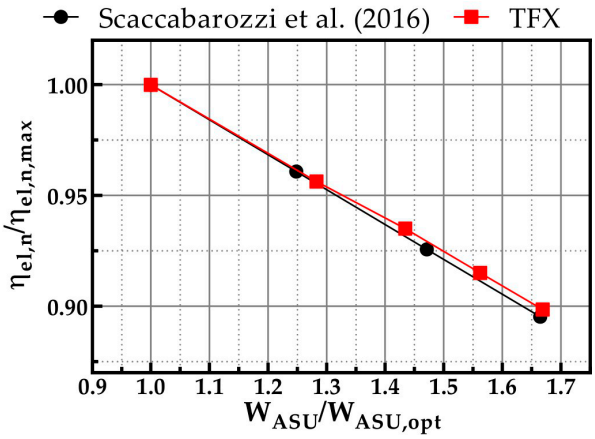

Figure 9. Net electric efficiency of the Allam cycle as a function of ASU-specific work. Validation against Scaccabarozzi et al., thermodynamic analysis, and numerical optimization of the NET Power oxy-combustion cycle [26].

3.2.1. Turbine Inlet Temperature

The effects of varying TIT from 1160 to 1255 °C on cycle performance can be inferred from Figure 5. Simulation results match very well those from [26]. The trend in $\eta_{el,n}$ showing an optimal value of TIT is confirmed (Figure 5a), unlike for Joule–Brayton cycles, where $\eta_{el,n}$ increases monotonically with TIT. According to [21,25,26], TIT_{opt} lies between 1150 and 1200 °C; in this study, it was found at 1200 °C.

The declining $\eta_{el,n}$ profile at TIT > TIT_{opt} can be attributed to a combination of the following factors:

1. Increase in the heat transfer irreversibility in the recuperator: the heat transfer through the heat exchanger (36), i.e., the first through which exhaust gases pass, is reduced, thus lowering $\eta_{el,n}$, in accordance with [26].
2. Increase of the turbine cooling flow rate: different from what is specified in [26], TIT augmentation was achieved by increasing the fuel mass flow rate at a constant recycling flow rate. Consequently, TIT grows with TOT and with coolant and recirculated CO_2 temperature. Although this latter effect could be beneficial to cycle efficiency, a higher amount of coolant is required to maintain the desired metal temperature. As discussed by El-Masri [30–32], the larger the coolant flow, the higher the thermo-fluid dynamic losses during the expansion phase, with consequent reduction in $\eta_{el,n}$.

Looking at Figure 5b, it seems that the Allam cycle behaves like traditional gas and steam cycles. W_n increases almost linearly with TIT, thanks to augmented expansion work. At TIT = 1200 °C, W_n equals 352 kJ/kg.

3.2.2. Turbine Inlet Pressure

TIP was varied from 220 to 340 bar, everything else being equal. In particular, both TIT and TOP were kept constant at 1158 °C and 31 bar, respectively. It is evident from Figure 6a that TIP is characterized by an optimal range where dimensionless $\eta_{el,n}$ curves reach a plateau. Indeed, $\eta_{el,n}$ is almost unchanged when TIP falls between 260 and 320 bar, consistent with [26]. In that range, the reduction in W_n caused by lowered TIP (Figure 6b) is somewhat compensated by an increase in TOT, thus enhancing heat recovery inside the recuperator. Improved regeneration has a beneficial effect on cycle efficiency, as recirculating CO_2 is fed into the combustor at higher temperature, and therefore, at a fixed TIT, a lower fuel input is required.

For TIP < 280 bar—especially below 260 bar—there is a strong drop in $\eta_{el,n}$ that might be explained through the heat transfer process in the recuperator. Specifically, reference is made to the heat exchangers labeled as (31) and (35) in Figure 2. Recirculating sCO_2, being compressed above its critical pressure (even for TIP below 260 bar) is affected by an increase

in c_p at low temperatures, which causes a thermal power deficit in the low-temperature section of the recuperator. This translates into an increase in pinch point and a reduction in heat transfer effectiveness with a negative impact on $\eta_{el,n}$.

Above 300–310 bar, TOT is reduced excessively, thus preventing the turbine exhaust from adequately preheating the recirculating CO_2, with consequent efficiency penalty. Moreover, an increase in flue gas temperature at the recuperator outlet was detected. What is described above agrees with the observations made in [26].

3.2.3. Turbine Outlet Pressure

TOP was varied between 20 and 35 bar: simulation outputs are depicted in Figure 7. An increase in TOP causes a linear reduction in turbine power output, hence in W_n (Figure 7b). Moreover, a decrease in the power absorbed by vapor phase compressors can be noticed because the pressure of the inlet recirculating CO_2 is closer to critical value. However, unlike what is reported in [26], the compression power of the dense phase pumps remained unchanged. The same is valid for pump inlet pressure, which in turns depends on CO_2 extraction pressure. This investigation also revealed the presence of an optimal TOP, around which the dimensionless curves are quite flat.

3.2.4. Turbomachinery Efficiency

For turbine stages, $\eta_{is,t}$ was varied from 80% to 95%, whereas the investigated range of $\eta_{is,c}$ for CO_2 compressors was between 78% and 95%. Raising $\eta_{is,t}$ by 1 percentage point led to an increase in $\eta_{el,n}$ by about 0.4 pp, which is much less than for a Brayton cycle (Figure 8a). This happens because boosting $\eta_{is,t}$ enhances the turbine power but decreases TOT. Therefore, there is less available thermal power for preheating recirculating CO_2 in the recuperator. Similarly, $\eta_{is,c}$ has a limited influence on $\eta_{el,n}$, compared with the Brayton cycle (Figure 8b), but the beneficial effect of raising $\eta_{is,c}$ on $\eta_{el,n}$ is confirmed. The reason why the Allam cycle is much less sensitive to compressors' performance can be found in the properties of the recirculating stream, which behaves like a real gas [26].

3.2.5. ASU Consumption

ASU specific work was varied between 972 and 1622 kJ/kg_{O2}. This is a fairly wide range, chosen for validation purposes. Figure 9 shows the strong negative impact of increasing ASU consumption on $\eta_{el,n}$. The linear declining trend is consistent with [26].

4. Cycle Optimization

The sensitivity analysis not only made it possible to validate the base-case model but also provided useful insight into the operating conditions of the simulated power plant. Based on the knowledge acquired, in order to improve the cycle performance at full load, multiple simulation sets were run for different levels of TIP, TIT, and TOP. In fact, these were selected as varying input parameters to maximize $\eta_{el,n}$, given the characteristics of ASU, compressors, and turbine described in the base case. Their mutual interaction was assessed with the help of "control loop" and "searcher" algorithms available in Thermoflex. The former tool was instructed to achieve the desired P_n of 300 MW within the tolerance of 0.25% by adjusting TIP and TOP. The specified range for turbine stage pressure ratio was [1.3; 1.5], whereas the pressure level for sink (12) and source (14) was set to change between 25 and 35 bar. Contextually, the latter was used as a support tool to optimization: a series of complete simulations were invoked using prospective values of TIT, set as the "adjuster" variable, in order to cause $\eta_{el,n}$, designated as the "target" output, to be maximized. The "searcher" uses the successive computed values of the target to guide further iterations in its search for the maximum target value. Two search processes were performed with a wide (first search) and narrow (second search) range for TIT variation (Figure 10).

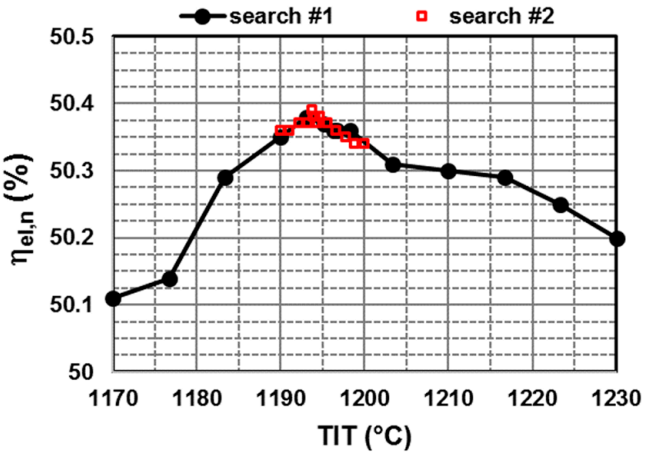

Figure 10. Search process of the maximum net electric efficiency of the Allam cycle as a function of turbine inlet temperature.

The procedure led to the establishment of a maximum $\eta_{el,n}$ of 50.4%, with P_n = 300.8 MW. This represents a modest but significant improvement compared with the base case, meaning that the operating parameters reported in [21,26] are already representative of a performance-driven configuration. Additional key parameters of the optimized cycle are reported in Table 3 for comparison with the base case. The optimization led to an approximately 3% increase in TIP, TIT, and TOT. Conversely, TOP was reduced by almost the same amount. This caused a rise in the power required by CO_2 compressors and pumps, although more than offset by the augmented turbine output. This grew by 6%, thanks to higher TIT and TIP, hence inlet enthalpy (1403 vs. 1352 kJ/kg), despite a slight increase in turbine outlet enthalpy (778 vs. 751 kJ/kg). In fact, the change in the turbine flow rate is negligible. The point is that turbine power grew more than fuel input, thanks to enhanced regeneration, because of higher TOT. Figure 11 shows the temperature-heat transfer diagram of the recuperator by putting in series heat exchangers 31, 35, and 36 (see Figure 2). Temperature differences at opposite ends are very small (2–5 °C), as it should be, whereas the value in between heat exchangers 35 and 36 is larger (49 °C). The burden of ASU remained practically unchanged, thus covering 87% of the total auxiliary consumption. Remaining fractions pertain to fuel compressor (5.5%), transformer losses (2.5%), and miscellaneous (5%).

Table 3. Comparison between Allam cycle configurations: base case vs. optimized case.

Parameter	Base Case	Optimized Case	Δ%
Turbine inlet pressure (bar)	292	303	3.8
Turbine inlet temperature (°C)	1158	1194	3.1
Turbine outlet pressure (bar)	31	30	−3.2
Turbine outlet temperature (°C)	706	728	3.1
Turbine coolant mass fraction (%)	11	12	–
Turbine exhaust flow (kg/s)	939	942	0.3
Expansion power (MW)	421	447	6.2
CO_2 compression power (MW)	70	73	4.3
Fuel input (MW)	574	597	4.0
Recuperator heat transfer (MW)	768	797	3.8
ASU penalty (%LHV)	10.64	10.66	0.2
Fuel compressor power (MW)	3.6	3.9	8.3
Net electric efficiency (%)	49	50.4	–
Net power output (MW)	281	301	7.1
Net specific work (kJ/kg)	335	358	6.9
Minimum cycle temperature (°C)	17	17	-

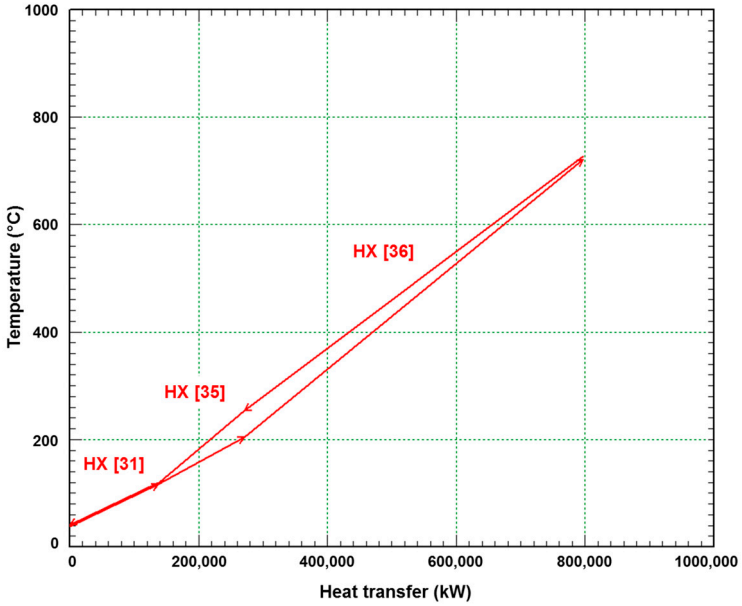

Figure 11. Temperature-heat exchanger diagram of the recuperator in the optimized case.

It is important to emphasize that P_n reached the target value of 300 MW with a 7% increase with respect to the base case. The same applies to W_n. The goal was achieved within the constraints of maximum allowable temperature at the hot end of the recuperator and at the turbine inlet, which is equal to 750 and 1200 °C, respectively [21].

5. Conclusions

A model of the NG-fired Allam cycle was conceived at full load for a power production of around 300 MW_{el}, consistent with the short-term construction of the first commercial unit by NET Power. This is a novel CO_2 oxyfuel power cycle that can inherently capture nearly all CO_2 emissions despite using a hydrocarbon fuel. A basic layout was designed as faithfully as possible to the information made public by the developers, with inclusion of data taken from published literature or engineering practice. Predictions deriving from a sensitivity analysis were successfully validated against previous theoretical studies, thus illustrating distinctive features of the Allam cycle, with respect to the Brayton cycle. An optimal value of TIT can be determined in the attempt of achieving the highest $\eta_{el,n}$, whereas profiles of $\eta_{el,n}$ as a function of TIP and TOP are quite flat around the maximum. As regards turbomachinery, the higher η_{is}, the greater the efficiency, albeit with a smaller impact compared with conventional gas turbine cycles.

The interdependence of these key thermodynamic parameters was assessed with the aim of enhancing the cycle performance at the design point. The objective function to be maximized is $\eta_{el,n}$, whereas the independent decision variables are TIT, TIP, and TOP. A gain in $\eta_{el,n}$ of 1.4 pp (from 49% to 50.4%) was achieved by raising TIT, TIP, and TOT by about 3%, thus taking advantage of increased turbine power and heat recovery through the recuperator.

This study lays the foundations for part load investigation of the Allam cycle behavior, given its role of zero-emission dispatchable technology. Without heat recovery from ASU, flexible options for oxygen supply could also be investigated from a technoeconomic perspective.

Author Contributions: Conceptualization, S.R.; methodology and software, L.C., A.S. and S.R.; validation and simulation, L.C. and A.S.; writing—original draft preparation, L.C., A.S. and S.R.; writing—review and editing, S.R.; supervision, S.R. All authors have read and agreed to the published version of the manuscript.

Funding: This research received no external funding.

Data Availability Statement: Not applicable.

Conflicts of Interest: The authors declare no conflict of interest.

Abbreviations

ASU	air separation unit
CCS	carbon capture and storage
c_p	specific heat capacity at constant pressure
cs	cooled surface interval
h	enthalpy
HX	heat exchanger
LHV	lower heating value
m	mass flow rate
NG	natural gas
NGCC	natural gas combined cycle
P	power
p	pressure
pp	percentage points
s	supercritical
T	temperature
Th	thickness parameter
th	coating thickness
TBC	thermal barrier coating
TFX	Thermoflex predictions
TIP	turbine inlet pressure
TIT	turbine inlet temperature
TOP	turbine outlet pressure
TOT	turbine outlet temperature
W	specific work
z	exponent
α	coefficient
ϕ	cooling effectiveness
γ	ratio of specific heat
η	efficiency
λ	thermal conductivity
μ	coefficient
Subscripts	
c	compressor
cf	coolant flow
el	electric
g	gas
in	inlet
is	isentropic
max	maximum
n	net
opt	optimal
out	outlet
t	turbine
th	thermal
TT	total-to-total
w	wall
y	polytropic

Appendix A

Table A1. Operating conditions related to numbered points in Figure 1 [21].

Stream Number	Temperature (°C)	Pressure (bar)
1	727	30
2	43	29
3	17	29
4	23	100
5	23	100
6	23	100
7	16	100
8	16	100
9	717	312
10	16	100
11	16	100
12	2	99
13	717	310
14	266	330

Table A2. Operating conditions related to stream numbers (see red and orange boxes) in Figure 2: base vs. optimized case.

	Base Case				Optimized Case			
Stream Number	p (bar)	T (°C)	h (kJ/kg)	m (kg/s)	p (bar)	T (°C)	h (kJ/kg)	m (kg/s)
1	212.1	1056.1	1209.8	882	218.1	1099.4	1270.3	873.6
2	154.3	974.3	1099.4	911.7	155.8	1009.1	1147.3	909.4
3	112.2	907.3	1009.9	930	110.5	935.5	1048.2	930.8
4	81.6	849.7	934.3	939.2	78.34	872.5	965	941.5
5	59.35	800.2	870.4	939.2	55.56	818.3	894.7	941.5
6	43.16	752.5	809.6	939.2	39.4	766.2	828	941.5
7	291.7	1158	1351.7	838.5	303.2	1193.8	1402.7	839.9
8	297.5	144	−27.81	881.7	309.2	204	68.34	881.7
9	297.5	144	−27.81	781.1	309.2	204	68.34	780.1
10	29	17	−103	939.2	28	17	−104.2	941.5
11	29	17	−39.52	913.7	28	17	−38.1	915
13	29	17	−39.58	909	28	17	−38.16	909
14	57.13	72.33	−2.908	909	49.45	62.82	−7.55	909
15	56.01	19.54	−94	909	48.48	19.54	−70.72	909
16	80	45.68	−81.39	909	78	57.13	−50.37	909
17	80	45.68	−81.39	27.27	78	57.13	−50.37	27.27
18	80	45.68	−81.39	881.7	78	57.13	−50.37	881.7
20	78.43	16	−270	690.7	76.47	16	−269.6	690.7
21	78.43	16	−270	191.1	76.47	16	−269.6	191.1
22	297.5	97.59	32.62	46.01	309.2	97.15	31.34	47.88
23	291.7	700.2	714.8	781.1	303.2	722.2	742.8	780.1
27	303.5	38.6	−238.5	881.7	315.4	116.9	−83.47	881.7
28	309.5	37.26	−241.3	881.7	321.7	38.54	−239.2	881.7
30	309.5	37.26	−241.3	690.7	321.7	38.54	−239.2	690.7
31	70	25	11.46	49,976	70	25	11.93	49,976
32	297.5	139	11.46	50,205	309.2	141.8	11.93	50,212
33	297.5	144	−27.81	21.65	309.2	204	68.34	18.55
34	31.39	706.1	750.9	939.2	30.31	727.5	778.8	941.5
35	309.5	37.26	−241.3	191.1	321.7	38.54	−239.2	191.1
36	297.5	144	−27.81	21.85	309.2	204	68.34	15.17
37	297.5	144	−27.81	13.39	309.2	204	68.34	17.86
38	29.58	39.26	−75.3	939.2	28.56	40.54	−74.98	941.5
39	297.5	144	−27.81	16.25	309.2	204	68.34	17.97
40	30.17	41.75	−72.68	939.2	29.13	118.9	70.83	941.5

Table A2. *Cont.*

	Base Case				Optimized Case			
Stream Number	**p (bar)**	**T (°C)**	**h (kJ/kg)**	**m (kg/s)**	**p (bar)**	**T (°C)**	**h (kJ/kg)**	**m (kg/s)**
41	30.78	172.3	127.1	939.2	29.71	253	214.4	941.5
42	297.5	144	−27.81	11.09	309.2	204	68.34	11.17
43	297.5	144	−27.81	16.45	309.2	204	68.34	20.95
44	297.5	144	−27.81	7.215	309.2	204	68.34	10.2
45	297.5	144	−27.81	6.174	309.2	204	68.34	5.976
46	297.5	144	−27.81	3.058	309.2	204	68.34	4.776
48	297.5	144	−27.81	40.92	309.2	204	68.34	49.98
49	297.5	144	−27.81	59.75	309.2	204	68.34	51.7

References

1. IEA. *Global Energy Review: CO_2 Emissions in 2021—Global Emissions Rebound Sharply to Highest Ever Level*; International Renewable Energy Agency: Paris, France, 2022.
2. Zakeri, B.; Paulavets, K.; Barreto-Gomez, L.; Echeverri, L.G.; Pachauri, S.; Boza-Kiss, B.; Zimm, C.; Rogelj, J.; Creutzig, F.; Ürge-Vorsatz, D.; et al. Pandemic, War, and Global Energy Transitions. *Energies* **2022**, *15*, 6114. [CrossRef]
3. Global Electricity Review 2022. Available online: https://ember-climate.org/insights/research/global-electricity-review-2022/ (accessed on 11 January 2023).
4. Holechek, J.L.; Geli, H.M.E.; Sawalhah, M.N.; Valdez, R. A Global Assessment: Can Renewable Energy Replace Fossil Fuels by 2050? *Sustainability* **2022**, *14*, 4792. [CrossRef]
5. Nuclear Energy and Sustainable Development. Available online: https://www.world-nuclear.org/information-library/energy-and-the-environment/nuclear-energy-and-sustainable-development.aspx (accessed on 11 January 2023).
6. Lau, H.C.; Ramakrishna, S.; Zhang, K.; Radhamani, A.V. The Role of Carbon Capture and Storage in the Energy Transition. *Energy Fuels* **2021**, *35*, 7364–7386. [CrossRef]
7. UNECE. *How Natural Gas Can Support the Uptake of Renewable Energy*; ECE ENERGY SERIES No. 66; United Nations: New York, NY, USA, 2019; ISBN 978-92-1-117229-4.
8. Sifat, N.S.; Haseli, Y. A Critical Review of CO_2 Capture Technologies and Prospects for Clean Power Generation. *Energies* **2019**, *12*, 4143. [CrossRef]
9. National Academies of Sciences, Engineering, and Medicine. *Advanced Technologies for Gas Turbines*; The National Academies Press: Washington, DC, USA, 2020. [CrossRef]
10. Allam, R.J.; Palmer, M.R.; Brown, G.W., Jr. System and Method for High Efficiency Power Generation Using a Carbon Dioxide Circulating Working Fluid. Assignee: 8 Rivers Capital LLC Palmer Labs LLC. U.S. Patent US8596075B2, 3 December 2013.
11. Rogalev, A.; Rogalev, N.; Kindra, V.; Zlyvko, O.; Vegera, A. A Study of Low-Potential Heat Utilization Methods for Oxy-Fuel Combustion Power Cycles. *Energies* **2021**, *14*, 3364. [CrossRef]
12. Crespi, F.; Gavagnin, G.; Sánchez, D.; Martínez, G.S. Analysis of the thermodynamic potential of supercritical carbon dioxide cycles: A systematic approach. *J. Eng. Gas Turbines Power* **2018**, *140*, 051701. [CrossRef]
13. Isles, J. Gearing up for a new supercritical CO_2 power cycle system. *Gas Turbine World* **2014**, *44*, 14–18.
14. NET Power Consolidates Business to Gear Up for Allam Cycle Power Plant Deployment. Available online: https://www.powermag.com/net-power-consolidates-business-to-gear-up-for-allam-cycle-power-plant-deployment/ (accessed on 12 January 2023).
15. Allam, R.J.; Palmer, M.R.; Brown, G.W., Jr.; Fetvedt, J.; Freed, D.; Nomoto, H.; Jones, C., Jr. High efficiency and low cost of electricity generation from fossil fuels while eliminating atmospheric emissions, including carbon dioxide. *Energy Procedia* **2013**, *37*, 1135–1149. [CrossRef]
16. Mancuso, L.; Ferrari, N.; Chiesa, P.; Martelli, E.; Romano, M. *Oxy-Combustion Turbine Power Plants*; IEAGHG report 2015/05; IEA: Paris, France, 2015.
17. Allam, R.J.; Fetvedt, J.E.; Forrest, B.A.; Freed, D.A. The oxy-fuel, supercritical CO_2 Allam Cycle: New cycle developments to produce even lower-cost electricity from fossil fuels without atmospheric emissions. In Proceedings of the ASME Turbo Expo 2014: Turbomachinery Technical Conference and Exposition, Düsseldorf, Germany, 16–20 June 2014.
18. Freed, D.; Forrest, B.; Patel, T.; Duffney, J. A Gas Turbine-driven, Integrally Gear Compressor solution: Enabling the Carbon Capture of the sCO_2 Allam Cycle Power Plant. In Proceedings of the 6th International Supercritical CO_2 Power Cycles Symposium, Pittsburgh, Pennsylvania, 27–29 March 2018.
19. Iwai, Y.; Itoh, M.; Morisawa, Y.; Suzuki, S.; Cusano, D.; Harris, M. Development approach to the combustor of gas turbine for oxy-fuel, supercritical CO_2 cycle. In Proceedings of the ASME Turbo Expo 2015: Turbomachinery Technical Conference and Exposition, Montreal, QC, Canada, 15–19 June 2015.
20. Nomoto, H.; Itoh, M.; Brown, W.; Fetvedt, J.; Sato, I. Cycle and Turbine Development for the Supercritical Carbon Dioxide Allam Cycle. In Proceedings of the International Conference on Power Engineering, Yokohama, Japan, 30 November–4 December 2015.

21. Allam, R.; Martin, S.; Forrest, B.; Fetvedt, J.; Lu, X.; Freed, D.; Brown, G.W.; Sasaki, T.; Itoh, M.; Manning, J. Demonstration of the Allam Cycle: An Update on the Development Status of a High Efficiency Supercritical Carbon Dioxide Power Process Employing Full Carbon Capture. *Energy Procedia* **2017**, *114*, 5948–5966. [CrossRef]
22. White, C.W.; Weiland, N.T. Evaluation of Property Methods for Modeling Direct-Supercritical CO_2 Power Cycles. *J. Eng. Gas Turbines Power* **2018**, *140*, 011701. [CrossRef]
23. Haseli, Y. Analytical Formulation of the Performance of the Allam Power Cycle. In Proceedings of the ASME Turbo Expo 2020: Turbomachinery Technical Conference and Exposition, Virtual, 21–25 September 2020.
24. Haseli, Y. Efficiency Maximization of Allam Cycle at a Given Combustion Temperature. In Proceedings of the ASME Turbo Expo 2021: Turbomachinery Technical Conference and Exposition, Virtual, 7–11 June 2021.
25. Haseli, Y. Approximate Relations for Optimum Turbine Operating Parameters in Allam Cycle. *J. Eng. Gas Turbines Power* **2021**, *143*, 064501. [CrossRef]
26. Scaccabarozzi, R.; Gatti, M.; Martelli, E. Thermodynamic analysis and numerical optimization of the NET Power oxy-combustion cycle. *Appl. Energy* **2016**, *178*, 505–526. [CrossRef]
27. Wimmer, K.; Sanz, W. Optimization and comparison of the two promising oxy-combustion cycles NET Power cycle and Graz Cycle. *Int. J. Greenh. Gas Control* **2020**, *99*, 103055. [CrossRef]
28. Mitchell, C.; Avagyan, V.; Chalmers, H.; Lucquiaud, M. An initial assessment of the value of Allam Cycle power plants with liquid oxygen storage in future GB electricity system. *Int. J. Greenh. Gas Control* **2019**, *87*, 1–18. [CrossRef]
29. Haseli, Y.; Sifat, N. Performance modeling of Allam cycle integrated with a cryogenic air separation process. *Comput. Chem. Eng.* **2021**, *148*, 107263. [CrossRef]
30. Rogalev, A.; Rogalev, N.; Kindra, V.; Komarov, I.; Zlyvko, O. Research and Development of the Oxy-Fuel Combustion Power Cycles with CO_2 Recirculation. *Energies* **2021**, *14*, 2927. [CrossRef]
31. Kindra, V.; Rogalev, A.; Lisin, E.; Osipov, S.; Zlyvko, O. Techno-Economic Analysis of the Oxy-Fuel Combustion Power Cycles with Near-Zero Emissions. *Energies* **2021**, *14*, 5358. [CrossRef]
32. El-Masri, M.A. On Thermodynamics of Gas-Turbine Cycles: Part 2—A Model for Expansion in Cooled Turbines. *J. Eng. Gas Turbines Power* **1986**, *108*, 151–159. [CrossRef]
33. El-Masri, M.A. GASCAN—An Interactive Code for Thermal Analysis of Gas Turbine Systems. *J. Eng. Gas Turbines Power* **1988**, *110*, 201–209. [CrossRef]
34. El-Masri, M.A. *Design of Gas Turbine Combined Cycles and Cogeneration Systems*; Thermoflow Inc.: Southborough, MA, USA, 2009; pp. 5.1–5.16.
35. Kolmetz Handbook of Process Equiment Design-Air separation units Selection, Sizing and Troubleshooting. Available online: https://www.klmtechgroup.com/PDF/EDG-SPE/ENGINEERING-DESIGN-GUIDELINES-air-separation-unit-Rev1.2web.pdf (accessed on 25 January 2023).